EUROPEAN ORGANIZATION FOR NUCLEAR RESEARCH

CERN-EP/80-97
11 June 1980

Backward K^{*0} Production in $\pi^- p \to \Lambda^0 K^+ \pi^-$ Reaction at 9 and 12 GeV/c

A. Ferrer[1], D. Treille
CERN, Geneva, Switzerland.

P. Rivet, A. Volte
Collège de France, 75005 Paris, France.

P. Benkheiri, G. de Rosny, A. Rougé
Ecole Polytechnique, 91128 Palaiseau, France.

B. Bouquet, B. d'Almagne, H. Nguyen, P. Petroff, F. Richard,
P. Roudeau, J. Six, H. Yoshida[2]
Laboratoire de l'Accélerateur Linéaire, 91405, Orsay, France.

ABSTRACT

We have analysed about 85000 fast Λ^0 events, obtained in a fast proton triggered experiment performed at the CERN-Ω Spectrometer at 9 and 12 GeV/c incident π^- beam. Nearly 2500 $\Lambda^0 K^+ \pi^-$ events have been isolated. We find strong production of quasi-two-body processes $\Lambda^0 K^{*0}$ and $\Sigma^{*-} K^+$ consistent with u-channel hyperon exchange. Results on Λ^0 polarisation, K^{*0} decay parameters and differential cross sections are given for $\Lambda^0 K^{*0}(892)$ and $\Lambda^0 K^{*0}(1430)$ final states. A comparison is made with the associate backward $\Lambda^0(1520) K^{*0}$ production seen in the four prong reaction $\pi^- p \to p K^- K^+ \pi^-$ obtained in the same experiment.

---

[1] On leave of absence from L.A.L. 91405 Orsay, France.

[2] Now at Fukui University, Fukui, Japan.

1. INTRODUCTION

We have measured the Λ^o polarisation, the K^{*o} decay parameters and the differential cross sections near the backward direction for the reactions

$$\pi^- p \to \Lambda^o K^{*o}(892) \quad (1)$$

$$\pi^- p \to \Lambda^o K^{*o}(1430 \quad (2)$$

at 9 GeV/c and 12 GeV/c incident π^- momenta.

The data of this work come from the fast-proton triggered experiment performed at the CERN-Ω Spectrometer[1-4]. Fast forward produced Λ^o were accepted by the trigger through their decay $\Lambda^o \to p_f \pi^-$. From a sample of about 85000 fast Λ^o identified events, a total of 1853 (616) candidates of reaction

$$\pi^- p \to \Lambda^o K^+ \pi^- \quad (3)$$

have been isolated by kinematical fits at 9(12) GeV/c. (See table 1). The detection efficiency of the recoiling $K^+\pi^-$ system in reaction (3) is good enough in the Ω Spectrometer to allow the measurement of the density matrix elements of the K^{*o}'s decays.

We have also investigated other quasi-two-body final states produced by hyperon exchange in this experiment, namely $\Sigma^{*-} K^+$ in the reaction (3) and $\Lambda^o(1520)$ K^{*o} in the four prong reaction:

$$\pi^- p \to p_f K^- K^+ \pi^- \quad (4)$$

2. EXPERIMENTAL CONDITIONS

The fast-proton experiment has already been described elsewhere (refs.1-4). The aim of this experiment was to carry out a systematic study of baryon exchange induced reactions. Let us recall here the essential features of the apparatus and trigger which have a definite importance for fast Λ^o reactions:

(i) Beam particles entering the Ω were identified by a set of three threshold Cerenkov counters. Their angle and position were measured with a set of five MWPC's located upstream the hydrogen target which was 30cm long and 3cm in diameter.

A cylindrical scintillation counter surrounded the target and was used in coincidence. This counter inhibits then the detection of neutral final state reactions $\pi^- p \to \Lambda^o K^o$ and $\pi^- p \to \Lambda^o K^{*o}$ with $K^{*o} \to$ neutrals.

(ii) Fast protons were selected using two high aperture threshold Cerenkov counters in anticoincidence located downstream from the Ω magnet, and their momenta were selected to be greater than half the beam momenta ($0.5\ p_{beam}$) by using two coincidence matrices[4].

The geometrical aperture of the fast proton counters allowed a good detection efficiency for protons with momenta greater than $0.5\ p_{beam}$ and emitted with $\theta_{lab} < 150$ mrad. These conditions ensure a good detection efficiency for fast $\Lambda^o \to p\pi^-$, with Λ^o momenta greater than $0.5\ p_{beam}$ and free of bias for Λ^o length of flight less than 150cm.

We must emphasize that this experiment was designed to trigger on fast proton events, and did not make use of the veto counter technique used in other fast Λ^o triggered experiments.

3. SELECTION OF THE EVENTS

3.1 Pattern Recognition and Geometrical Reconstruction

All the fast proton triggers recorded (see table 1) were processed through our version of ROMEO (Ω Pattern Recognition and Geometry Program). The reconstructed events were treated by a vertex finding and fitting program that we developed to find primary as well as secondary V^o vertices. The main criteria used in the V^o finding program consisted of:

(i) Clear geometrical separation of the main vertex and the V^o vertex
(ii) Compatibility of the V^o mass with the Λ^o mass assignment within errors.

The Λ^o mass distribution is centered at the Λ^o mass, and its full width at half maximum is 7.2 MeV. Only topologies with at least one charged track

in the main vertex have been retained: the total number of V^o candidates with a mass inside the bounds (1.105, 1.125) GeV is given in table 1. The background under the selected sample of reconstructed Λ^o is negligible.

The most important source of Λ^o losses come from the Λ^o geometrical reconstruction. They are clearly visible in the Λ^o length of flight distribution: ℓ_Λ. By studying a sample of simulated data through the SIMEGA-PLUMEGA-ROMEO chain of programs[4], we computed the efficiency $\varepsilon(\ell_\Lambda)$, of Λ^o reconstruction as a function of ℓ_Λ (Fig. 1). The important losses for $\ell_\Lambda < 60$cm are due to the fact that fast Λ^o's are very difficult to separate geometrically from the main vertex interaction: Events with $65 < \ell_\Lambda < 140$cm are reconstructed with a high and uniform efficiency, and we have used this result to check all our cross sections calculations. Finally for Λ^o's with $\ell_\Lambda > 140$cm the efficiency decreases very fast: this is due to the combined effect of short measurable track length in the Ω chambers and to the fast proton counters geometrical acceptance.

We have also investigated other possible detection losses. The angular decay distribution of the proton with respect to the Λ^o line of flight, in the Λ^o rest frame has been found compatible with isotropy as expected. Taking into account the efficiency $\varepsilon(\ell_\Lambda)$ we performed a maximum likelihood fit to compute the Λ^o lifetime. Our results, verified for different length of flight interval cuts, are consistent with the world average Λ^o lifetime value[5] $\tau = (2.632 \pm 0.020) \times 10^{-10}$ sec. In particular, when selecting only Λ^o candidates with $65 < \ell_\Lambda < 140$cm (13402 events), we obtain:

$$\tau_\Lambda = (2.568 \pm 0.063) \times 10^{-10} \text{ sec.}$$

3.2 Kinematical Fits

The reaction in which we are interested here

$$\pi^- p \to \Lambda^o K^+ \pi^- \qquad (3)$$

can be observed in the Ω Spectrometer in the two following final state topologies

$$\Lambda^o + 1 \text{ prong} \qquad (3a)$$

$$\Lambda^o + 2 \text{ prongs} \qquad (3b)$$

Events with either a π^- or a K^+ missing in the primary vertex (3a) are due

to the limited geometrical acceptance of the Ω spark chambers or to ROMEO program inefficiencies. Consequently we selected the events with topologies (3a) and (3b) to extract the candidates for reaction (3). To this purpose, we used the program KOMEGA, which is a kinematic fit program adapted for Ω events, in a two step process. First we tried a 3-C fit to select good Λ^o events. About 90% of the candidates gave a good 3-C Λ^o fit. Second, using the previous Λ^o fit result plus the incoming and outgoing charged tracks in the main vertex as measured by ROMEO, we tried 1-C fits or 4-C fits for topologies (3a) or (3b) respectively.

a) 4-C fits for the Λ^o + 2 prongs topology

Events with charge balanced Λ^o + 2 prongs topology were used to try 4-C fits to hypothesis (3). About 4% of the candidates satisfied a good kinematical fit with χ^2 probability > 1%.

b) 1-C fits for the Λ^o + 1 prong topology

This category of events contains good candidates of reaction (3) where either the "slow" π^- or K^+ is undetected.

Taking into account the resolution in the measurement of a missing particle we first plotted the missing mass spectra for the events with a negative (positive) particle missing in the main vertex. We observed the expected bump at the pion (kaon) mass. In order to optimise the signal/background ratio we restricted our samples with the requirement that the missing mass squared MM^2 to the hypothesis $\Lambda^o\pi^-(MM_+)$ and $\Lambda^oK^+(MM_-)$ is such as:

$$-.1 < MM_+^2 < .3 \text{ GeV}^2$$

$$-.22 < MM_-^2 < .08 \text{ GeV}^2$$

These cuts introduce a loss of good events that we estimated to be 28 ± 3% and 42 ± 3%, and the remaining background was found $\leq$ 10% and $\leq$ 7% respectively.

Apart from doubling our statistics, these 1-C events allow us to verify our acceptance calculations. The final statistics available can be seen in table 1.

4. DATA ANALYSIS

4.1 General Review of the Mass Spectra

We show in Fig. 2 the Dalitz plot $M^2(\Lambda^o\pi^-)$ versus $M^2(K^+\pi^-)$ for the 9 GeV/c and 12 GeV/c data. We observe two clear accumulations in the $K^{*o}892$ and $K^{*o}1430$ regions, and a strong density of events in the low $\Lambda^o\pi^-$ mass region. The two invariant mass projections are presented in Fig. 3, for the $\Lambda^o\pi^-$ system and in Fig. 4 for the $K^+\pi^-$ system.

Among the three peaks visible at low $\Lambda^o\pi^-$ mass values (Fig. 3), only the first one can unambiguously be assigned to the well known $\Sigma^-(1385)$ hyperon. The two other peaks are 3 to 4 standard deviation effects above the background, and one could temptatively assign them to the $\Sigma^-(1670)$ $J^P = 3/2^-$ and $\Sigma^-(1915)$ $J^P = 5/2^+$ I = 1 hyperons(*). It is important to note that these peaks remain even when we subtract the K^{*o} signals (dotted curves in Fig. 3). However, the background under these hyperons is so important that we cannot properly analyse their production and decay properties. Also we suspect that some remaining Σ^o background coming from $\pi^-p \to \Sigma^oK^+\pi^-$ reaction could contribute to those signals.

In the $K^+\pi^-$ invariant mass spectra (Fig. 4) we see a strong $K^{*o}(892)$ and a clear $K^{*o}(1430)$ signal. This experiment reports, for the first time, the production properties and backward cross sections for the $K^{*o}(1430)$ meson in reaction (3).

For completeness we show in Fig. 5 the Λ^oK^+ invariant mass spectra, where no N^{*+} baryon seems to be present.

4.2 Study of Quasi-Two-Body Processes

The quasi-two-body processes present in reaction (3) can be classified according to three different baryon exchange diagrams as shown in Fig. 6,

---

* These J^P assignments are suggested by the spin parity series of the baryons $\Delta(1236)$, $N^*(1520)$ and $N^*(1688)$ seen in our experiment in the quasi-two body Nucleon-exchange reactions:
$\pi^-p \to N^{*o}\pi^o(11)$ as well as $\pi^-p \to N^{*o}\rho^o$, $N^{*o}f^o(4)$ and $\pi^-p \to N^{*o}\omega^o(12)$.

where the first diagram accounts for backward production of K^{*o} mesons. Here only the quantum numbers of the Σ-hyperon can be exchanged. Mechanism (II) can be associated to the production of Σ^{*-} forward hyperons, and therefore both $I_u = 0$, 1 isospin in the u-channel can be exchanged. Finally, mechanism (III) could explain the production of $N^{*+} \to \Lambda^o K^+$ via $I_u = 3/2$ exchange (Δ baryon exchange); unfortunately the ΛK partial decay modes of the N*'s are not very well known, and the small number of events that we obtained in the low mass $\Lambda^o K^+$ mass spectra make insensitive any conclusion on this mechanism.

4.2.1 Backward K^{*o} Production

The two clear signals visible in Fig. 4, show the backward production of K*892 and K^{*o}1430 mesons, via the mechanism (I) of Fig. 6.

We have fitted the $K^+\pi^-$ mass spectrum of Fig. 4 using a parametrization of the form

$$f(M) = (M-M_1)^{\frac{1}{2}} P(M) \ (1 + BW_1 + BW_2) \qquad (5)$$

where M_1 is a constant, fixed at the $K^+\pi^-$ mass threshold, P(M) is a polynomial in M with free parameters representing the phase space and the detection acceptance variation as a function of M, and the two Breit-Wigner functions BW_i account for the K^{*o} resonances. The mass and width of each BW_i function were left free in the fit, and the best results have been reported in table 2. We obtain lower values for the masses of these resonances than those reported by the Particle Data Group[5], mainly for the K*(1430) and probably due to a systematic effect in our two-step kinematical fit procedure.

Our purpose here will be to analyse the production properties as well as the Λ^o polarisation and the K^{*o} decay parameters and verify if the simple hyperon exchange mechanism is consistent with our data.

We have selected the samples of backward K^{*o} events according to the following $K^+\pi^-$ mass cuts:

$$K^{*o}(892) \quad 770 \leq M(K^+\pi^-) \leq 1100 \text{ MeV}$$
$$K^{*o}(1430) \quad 1320 \leq M(K^+\pi^-) \leq 1520 \text{ MeV}$$

The u' production distributions ($u' = u_{max} - u$, u being the momentum transfer squared from the incident π^- to the outgoing fast Λ^o) are shown in Fig. 7. We observe an accumulation of events at small u' values. We verified that both the trigger acceptance and the Ω optical chambers acceptance do not affect these distributions (in the u' range considered here, we find variations of the order of 1 to 2%). In Fig. 7 we have also drawn the best exponential fits obtained to the experimental u' distributions.

A detailed analysis of the K^{*o} acceptance was performed with a quasi-two-body Monte-Carlo simulation program. No bias in the K^{*o} angular distributions was detected in this analysis. We therefore computed the density matrix elements ρ_{ij} for the K^{*o}'s decays using as analyser the K^+ decay angle in their respective u-helicity Jackson frames.

The $K^{*o}(892)$ density matrix elements were obtained using the known $J^P = 1^-$ decay angular distribution[10] and applying the moments method. For this calculation only the most backward K^{*o} events were selected, e.g. those satisfying $u' < 0.5$ GeV^2. Our results (table 3) show that all allowed spin projections are present. The ρ_{ij} values reported were obtained after background subtraction, using events in both sides of the K^{*o} mass intervals. However our results do not vary strongly with or without background subtraction.

The angular decay distribution for the $K^{*o}(1430)$ meson was analysed with the known $J^P = 2^+$ angular decay distribution, using also the moments method. Table 4 shows the results obtained. We note that the matrix elements ρ_{ij} with i or j equal 2 are negligible, implying that helicity-2 decay is depressed in our data. This result is in agreement with the simple idea of Σ-exchange dominant mechanism (Fig. 6).

We computed the Λ^o polarisation for each sample of K^{*o} events according to the formula

$$P = \frac{1}{\alpha} \frac{\langle \cos\theta \rangle}{\langle \cos^2\theta \rangle}$$

where $\alpha = 0.642$, is the Λ^o decay asymmetry parameter, and θ is the angle between the decay proton direction in the Λ^o rest frame and the normal to

the production plane. Our results are plotted in Fig. 8 as a function of u'. They are compatible with the available data[7], and show that the Λ^o polarisation is positive in the backward region, like in the $\Lambda^o K^o$ final state. Concerning the dip observed around u' = .1 by Brundiers et al., (Ref. 7), our statistics are too low to confirm it.

To compute backward cross sections we have used the same method already published in a previous work[4] to convert events into cross sections. In addition, we have calculated the following effects:

Λ^o losses by scattering in the target and chambers
losses due to missing mass cuts to select 1-C candidates
K^{*o} and Λ^o branching ratios
losses due to K^{*o} mass cuts
Λ^o losses in the analysis programs.

We used the nominal sensitivity given in table 1, that includes beam attenuation corrections, and we applied the same method as described in Ref. (4) to correct for ROMEO inefficiencies and to deal correctly with geometrical acceptance of the trigger and the Ω optical chambers. The global acceptances are high (> 50%) for u' < 1 GeV^2, and the corrections to be applied are not very important. Finally the estimated Σ^o contamination and the remaining background under the K^{*o} signals has been subtracted according to the results on the mass fits and the total backward cross sections obtained in our experiment are given in table 5.

In order to compare our results on the $K^{*o}892$ cross sections with the existing data[6-9], we have plotted in Fig. 9 the compilation of K^{*o} cross sections integrated in the u' < 0.3 GeV^2 range. A good linear fit is obtained, and a parametrisation of the form $\sigma \sim s^{-n}$ gives $n = +3.15 \pm 0.15$. Under the hypothesis that a simple Regge trajectory gives rise to this energy variation through a dependence $s^{2\alpha_o - 2}$, we obtain $\alpha_o \simeq -.6$, a value sitting between the known Σ hyperon trajectories $\Sigma_\alpha - \Sigma_\gamma$ $(-.86 \pm 0.9u)$ and $\Sigma_\delta - \Sigma_\beta (-.30 \pm 0.9u)$[13].

The presence of these two exchanges has been established by Ward et al[9] in their study of the energy dependence of $\pi^- p \to \Lambda^o K^o$ reaction cross section near u' = 0.

4.2.2 Σ* Production

It is clear from Fig. 3 that, there are three enhancements in the low $\Lambda^{o}\pi^{-}$ invariant mass spectrum, despite the fact that they lie over an important background ($\geq$ 50%).

We fitted the $\Lambda^{o}\pi^{-}$ mass spectrum of Fig. 3 using a similar parametrisation formula as that given in (5). The results on the mass and width of each of the three Breit-Wigner functions have been reported in table 2.

The first signal corresponds to the $\Sigma^{-}(1385)$, $J^{P} = 3/2^{+}$ hyperon, and the production mechanism should correspond to diagram (II) of Fig. 6.

Unfortunately, we do not have enough statistics and the background level is too high to analyse precisely this low mass hyperons. We limited our analysis to study the acceptance of our trigger and the Ω chambers for the three hyperons assuming an isotropic decay distribution.

The global acceptance for the $\Sigma^{-}(1385)$ is very good in the whole $\Lambda^{o}\pi^{-}$ angular decay distribution. The fast proton trigger acceptance depletes about half of the angular distribution for the $\Sigma^{-}(1670)$ decay, and this is still more pronounced for the $\Sigma^{-}(1915)$ decay.

Under the hypothesis of a uniform decay angular distribution (which is in agreement with the data, at least for the $\Sigma^{-}(1385)$, and a production mechanism following the law $d\sigma/du' \sim \exp(-3u')$, we obtain the total backward cross sections given in table 5.

4.3 Backward K^{*o} Production in the Four Body $\pi^{-}p \to p_f K^{-} K^{+} \pi^{-}$ Reaction

Here we report on the backward production of K^{*o} mesons via the quasi-two-body reaction

$$\pi^{-}p \to \Lambda^{o}(1520)\ K^{*o} \qquad (6)$$

with the subsequent decay $\Lambda^{o}(1520) \to p_f K^{-}$.

The fast proton reaction

$$\pi^{-}p \to p_f K^{-} K^{+} \pi^{-} \qquad (4)$$

for which we have already reported inclusive results[3], has been obtained

from kinematical 4-C fits on the four prong charge balanced topology sample. A total of 525 events at 12 GeV/c and 909 events at 9 GeV/c were used for this analysis.

Fig. 10 shows the invariant masses $p_f K^-$ and $K^+\pi^-$, for the 9 GeV/c data only, where we can see the $\Lambda^o(1520)$ and $K^{*o}(892)$ signals respectively. If furthermore, we select the 96 events for which the $p_f K^-$ mass lies in the $\Lambda^o(1520)$ bin, we obtain the $K^+\pi^-$ mass spectrum shown in Fig. 11. Here we have used both 9 and 12 GeV/c data samples as our statistics is very low. We observe in Fig. 11 that both $K^{*o}(892)$ and $K^{*o}(1430)$ appear to be produced backwards in reaction (6).

The production mechanism of reaction (6) should follow the Σ-exchange as illustrated in diagram (I) of Fig. 6. We computed the cross sections for these channels - backward $K^*(892)$ and $K^{*o}(1430)$ -, by using the method described in ref.(4) and after all corrections were applied, we obtained the results given in table 5. These cross sections were corrected for all branching ratios. However they are model dependent in the sense that the unobserved events were corrected by simulating through our quasi-two-body Monte Carlo program the reactions (6) with the hypothesis that the $\Lambda^o(1520) \to pK^-$ decay is isotropic, and that the production $d\sigma/du'$ law follows an exp $(-3u')$ distribution.

CONCLUSIONS

We have investigated backward K^{*o} production in quasi-two-body reactions from data obtained in the fast proton triggered experiment done at the Ω Spectrometer. We have mainly used Λ^o_f events, selecting from these data about 85000 fast Λ^o candidates, then extracting a total of 2500 events of reaction $\pi^- p \to \Lambda^o K^+ \pi^-$ at 9 and 12 GeV/c incident momenta.

Our conclusions on this analysis are the following:

1. A strong quasi-two-body production of $K^{*o}892$ and $K^{*o}1430$ in the backward region is present in the data.
2. The polarisation of the Λ^o is clearly positive for both $K^{*o}(892)$ and $K^{*o}(1430)$ channels.

3. This backward production of K^{*o} is consistent with a Σ-exchange mechanism but our data does not disentangle which are the dominant trajectories, e.g. whether $\Sigma_\alpha - \Sigma_\gamma$ or $\Sigma_\beta - \Sigma_\delta$ trajectories.

4. The analysis of the four prong reaction $\pi^- p \to pK^- K^+ \pi^-$ shows evidence for backward K^{*o} production in the quasi-two-body reactions $\pi^- p \to \Lambda^o(1520)\ K^{*o}(892)$ and $\Lambda^o(1520)\ K^{*o}(1430)$, with similar cross sections as those found for the channels associated with the $\Lambda^o(1115)$.

REFERENCES

1. J. Boucrot et al., Nucl. Phys. B121 (1977) 251.

2. A. Jacholkowski et al., Nucl. Phys. B126 (1977) 1.

3. T. Hofmokl et al., Nucl. Phys. B129 (1977) 19.

4. A. Ferrer et al., Nucl. Phys. B142 (1978) 77.

5. Particle Data Group, Review of Particle Properties, Phys. Lett. 75B (1978) 1.

6. K.J. Foley et al., Phys. Rev. D10 (1974) 2763.

7. H. Brundiers et al., Nucl. Phys. B119 (1977) 349.

8. D.L. Scharre. Ph.D. Thesis. LBL-6149 (1977).

9. C.E.W. Ward et al., Phys. Rev. D16 (1977) 2041.

10. J.D. Jackson, Nuovo Cim 34 (1964); K. Gottfried and J.D. Jackson, Nuovo Cim. 33 (1964) 309.

11. A. Rougé et al., Phys. Letters 69B (1977) 115.

12. P. Benkheiri et al., Nucl. Phys. B150 (1979) 268.

13. V. Barger, D. Cline and J. Matos, Phys. Letters 29B (1969) 121.

FIGURE CAPTIONS

Fig. 1: Λ^o total reconstruction efficiency $\varepsilon(\ell_\lambda)$ as a function of its length of flight ℓ_Λ.

Fig. 2: $\Lambda^o K^+ \pi^-$ final state Dalitz-plot.

Fig. 3: Invariant mass $\Lambda^o \pi^-$. Dotted line, $K^{*o}(892)$ and $K^{*o}(1430)$ events subtracted.

Fig. 4: Invariant mass $K^+ \pi^-$. Dotted line, $M(\Lambda^o \pi^-) < 2$ GeV/c events subtracted.

Fig. 5: Invariant mass $\Lambda^o K^+$.

Fig. 6: Baryon exchange diagrams referred in the text.

Fig. 7: u' distributions for backward $K^{*o}892$ and $K^{*o}1430$. (9 GeV/c data).

Fig. 9: Backward $K^{*o}892$ cross section compilation as function of P_{LAB}.

Fig. 10: $p_f K^-$ and $K^+ \pi^-$ invariant masses from $\pi^- p \to p_f K^+ K^- \pi^-$ reaction. (9 GeV/c data).

Fig. 11: $K^+ \pi^-$ invariant mass for $\pi^- p \to \Lambda^o(1520)\ K^+ \pi^-$ events. The curve is the best fit to the data.

TABLE 1

Summary of selected events		9 GeV/c	12 GeV/c
number of triggers		1.6×10^6	1.1×10^6
nominal sensitivity		9400 evts/μb	5800 evts/μb
total fast Λ^o reconstructed		60606	25800
Λ^o + 1 prong		15871	6873
Λ^o + 2 prongs		25209	11382
$\Lambda^o K^+ \pi^-$ events	1-C fits	1028	319
	4-C fits	825	297

TABLE 2

Mass (M) and width (Γ) of the Breit-Wigner functions that give the best fit to the $K^+\pi^-$ and $\Lambda^o\pi^-$ mass spectra, as explained in the text (9 GeV/c data only).

	M (MeV)	Γ (MeV)		M (MeV)	Γ (MeV)
$K^{*o}(892)$	888 ± 3	63 ± 9	$\Sigma^-(1385)$	1380 ± 7	70 ± 10
$K^{*o}(1430)$	1385 ± 10	103 ± 30	$\Sigma^-(1670)$	1668 ± 10	90 ± 20
			$\Sigma^-(1915)$	1910 ± 17	87 ± 25

TABLE 3

$K^{*o}(892)$ decay density matrix elements in u-helicity Jackson frame

	No.of events (weighted)	ρ_{00}	$\rho_{11}+\rho_{1-1}$	$\rho_{11}-\rho_{1-1}$	ρ_{10}
9 GeV/c	507	.33 ± .05	.49 ± .05	.19 ± .04	.07 ± .03
12 GeV/c	185	.31 ± .10	.48 ± .09	.21 ± .08	.07 ± .05

TABLE 4

$K^{*o}(1430)$ decay density matrix elements in u-helicity Jackson frame

	No.of events (weighted)	ρ_{00}	$\rho_{11}+\rho_{1-1}$	$\rho_{11}-\rho_{1-1}$	$\rho_{22}+\rho_{2-2}$	$\rho_{22}-\rho_{2-2}$
9 GeV/c	381	.34±.05	.24±.04	.37±.04	.02±.04	.03±.04
12 GeV/c	88	.36±.11	.19±.10	.25±.11	.16±.09	.03±.09

	$\mathrm{Re}\,\rho_{21}$	$\mathrm{Re}\,\rho_{2-1}$	$\mathrm{Re}\,\rho_{20}$	$\mathrm{Re}\,\rho_{10}$
9 GeV/c	-.08±.02	-.02±.02	-.03±.02	-.10±.03
12 GeV/c	-.09±.05	-.05±.05	-.07±.06	-.05±.06

TABLE 5

Total backward cross sections

Channel	9 GeV/c (μb)	12 GeV/c (μb)
$\pi^- p \to \Lambda^0(1115)\ K^{*0}(892)$	0.39 ± 0.05	0.16 ± 0.05
$\Lambda^0(1115)\ K^{*0}(1430)$	0.47 ± 0.10	0.20 ± 0.09
$\pi^- p \to \Lambda^0(1520)\ K^{*0}(892)$	0.48 ± 0.14	0.16 ± 0.09
$\to \Lambda^0(1520)\ K^{*0}(1430)$	0.46 ± 0.18	0.19 ± 0.10
$\pi^- p \to \Sigma^-(1385)\ K^+$	0.06 ± 0.02	0.03 ± 0.01
$\Sigma^-(1670)\ K^+$	0.07 ± 0.03	0.04 ± 0.03
$\Sigma^-(1915)\ K^+$ $\hookrightarrow \Lambda^0\pi^-$	0.10 ± 0.04	0.05 ± 0.04

The K^{*0} cross sections are corrected for isospin and branching ratio of both K^{*0} and Λ^0 decays. For the $\Lambda(1520)$ decay in $N\bar{K}$, we have used the ratio .46 ± .01 given in Ref.(5).

The Σ^- cross sections have not been corrected neither for $\Lambda^0\pi^-$ nor for Λ^0 decay branching ratios. The errors are only statistical and do not include an overall normalisation uncertainty of 15%.

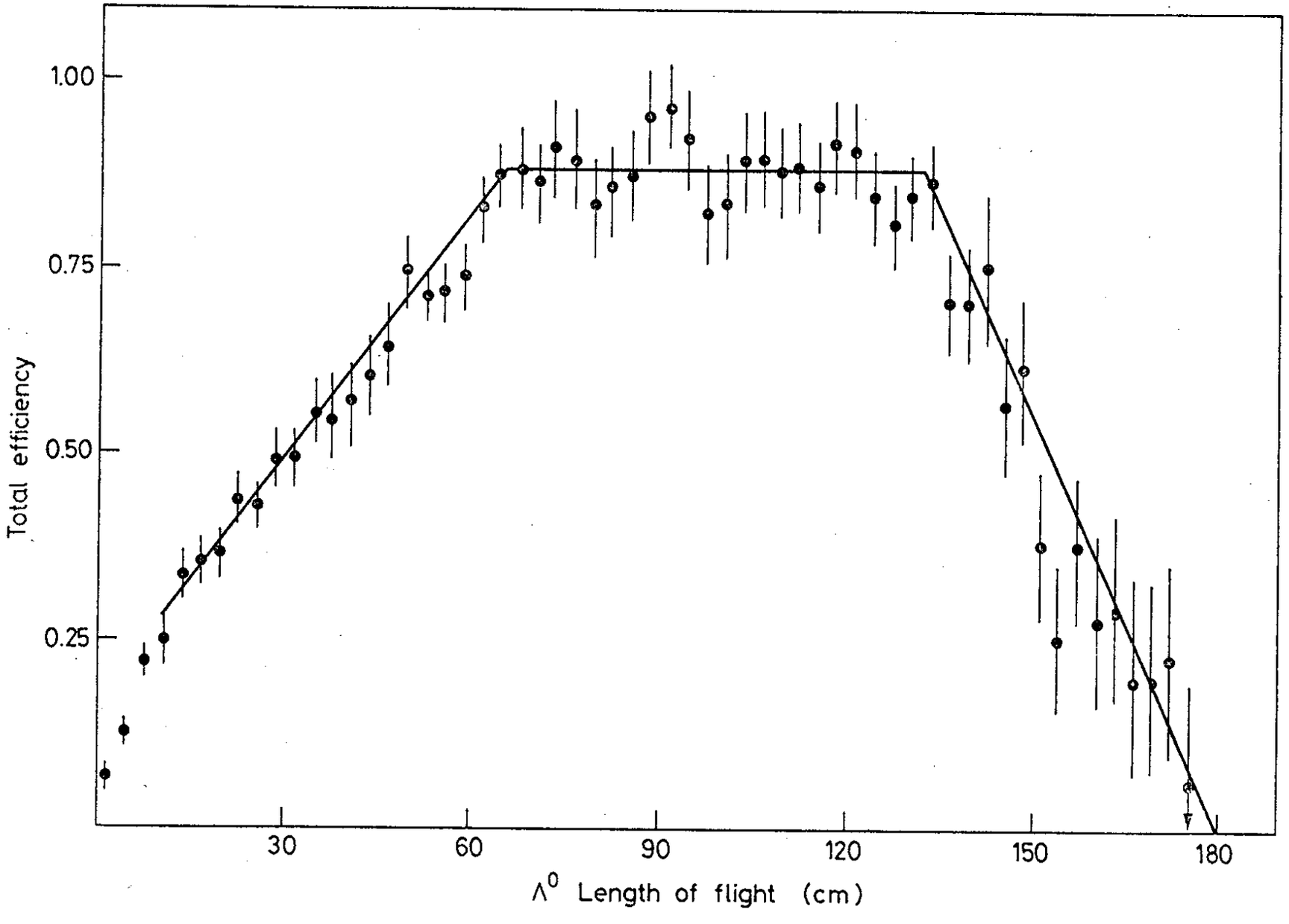
1.00
0.75
0.50
0.25
Total efficiency
30
60
90
120
150
180
Λ⁰ Length of flight (cm)

FIG. 1

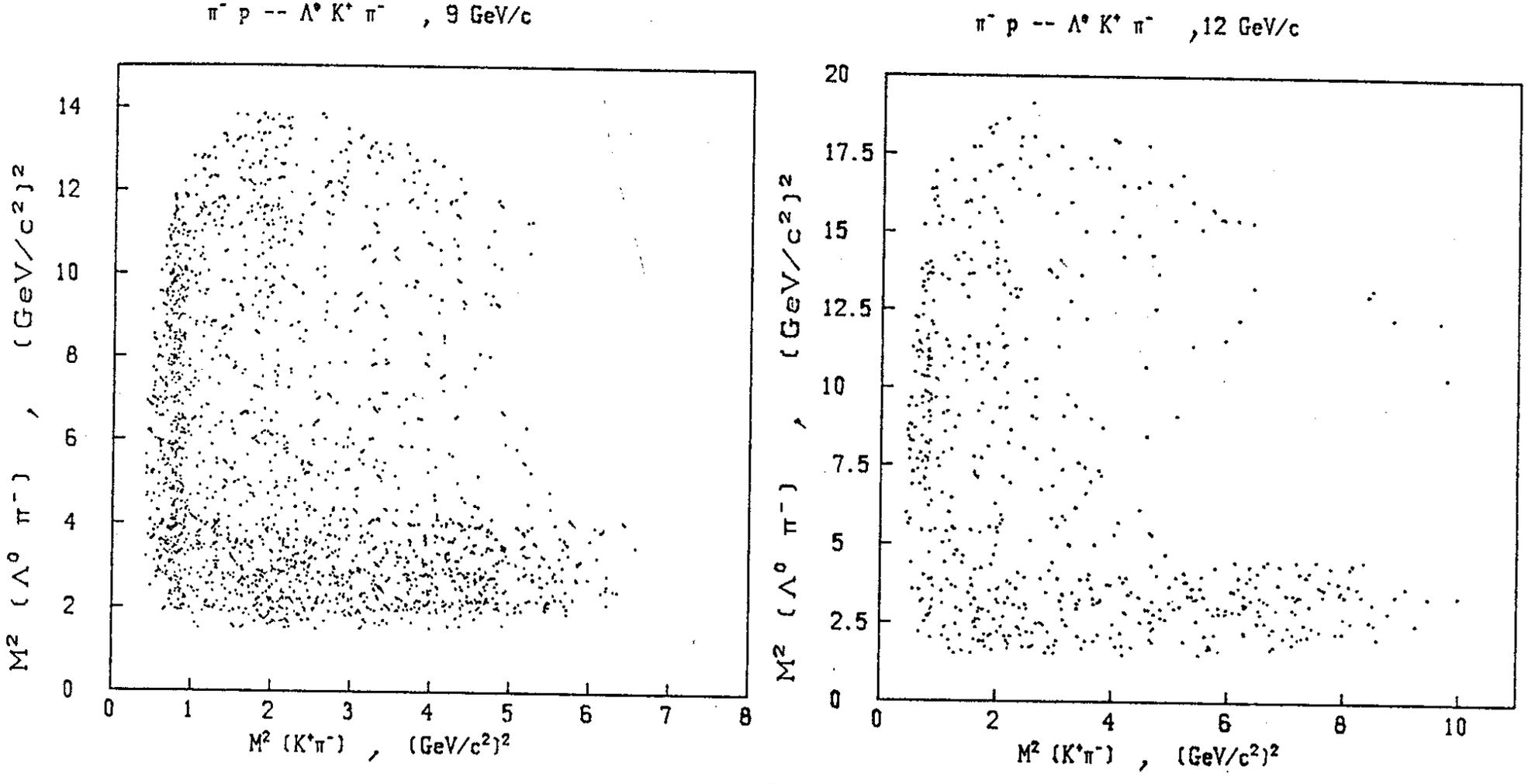
π⁻ p -- Λ° K⁺ π⁻ , 9 GeV/c
M² (Λ° π⁻) , (GeV/c²)²
M² (K⁺π⁻) , (GeV/c²)²
0
2
4
6
8
10
12
14
1
3
5
7
π⁻ p -- Λ° K⁺ π⁻ ,12 GeV/c
M² (Λ° π⁻) , (GeV/c²)²
M² (K⁺π⁻) , (GeV/c²)²
2.5
7.5
12.5
15
17.5
20

FIG.2

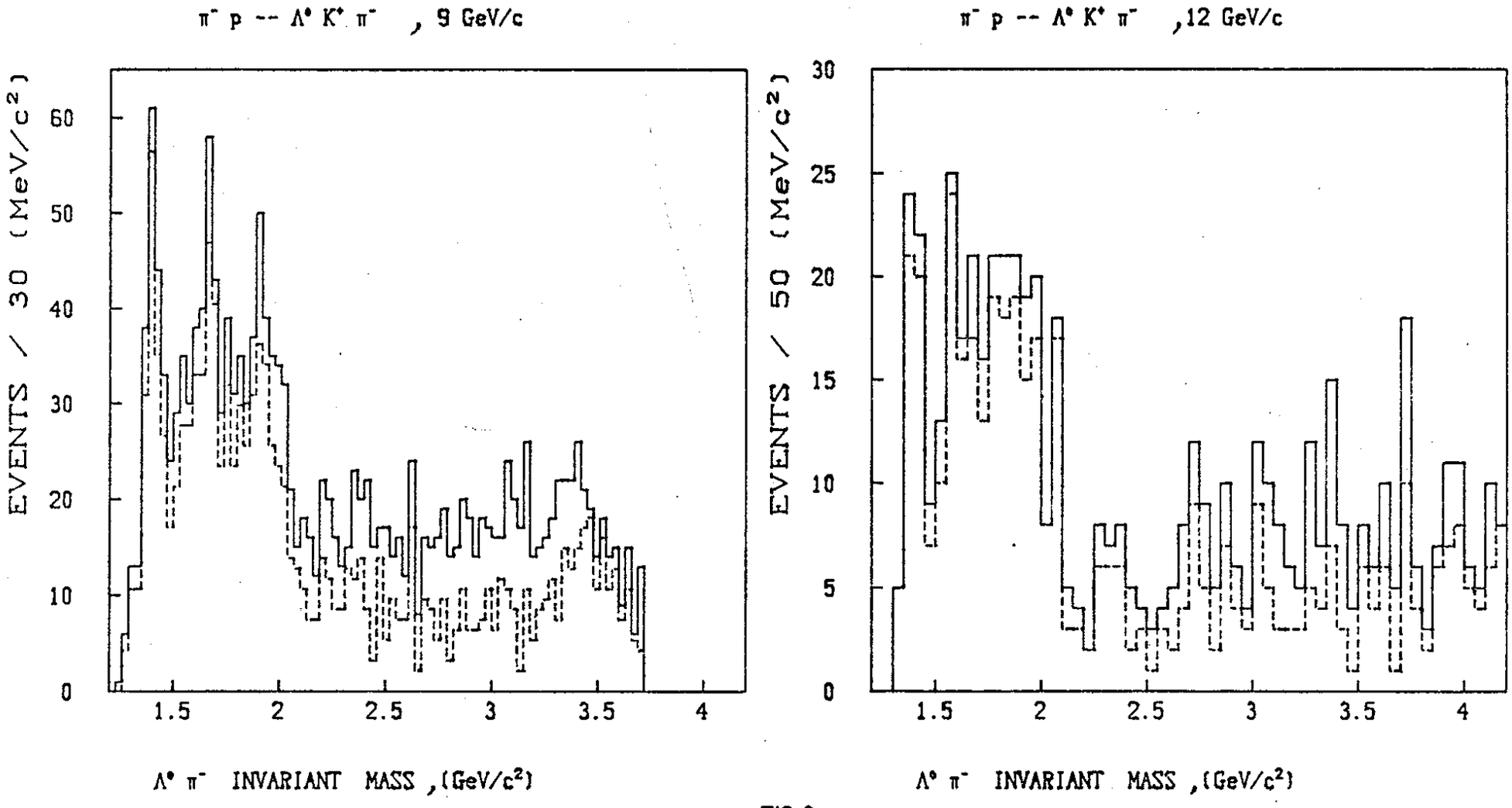
π⁻ p -- Λ° K⁺ π⁻ , 9 GeV/c
EVENTS / 30 (MeV/c²)
0
10
20
30
40
50
60
1.5
2
2.5
3
3.5
4
Λ° π⁻ INVARIANT MASS ,(GeV/c²)
π⁻ p -- Λ° K⁺ π⁻ ,12 GeV/c
EVENTS / 50 (MeV/c²)
0
5
10
15
20
25
30
1.5
2
2.5
3
3.5
4
Λ° π⁻ INVARIANT MASS ,(GeV/c²)

FIG.3

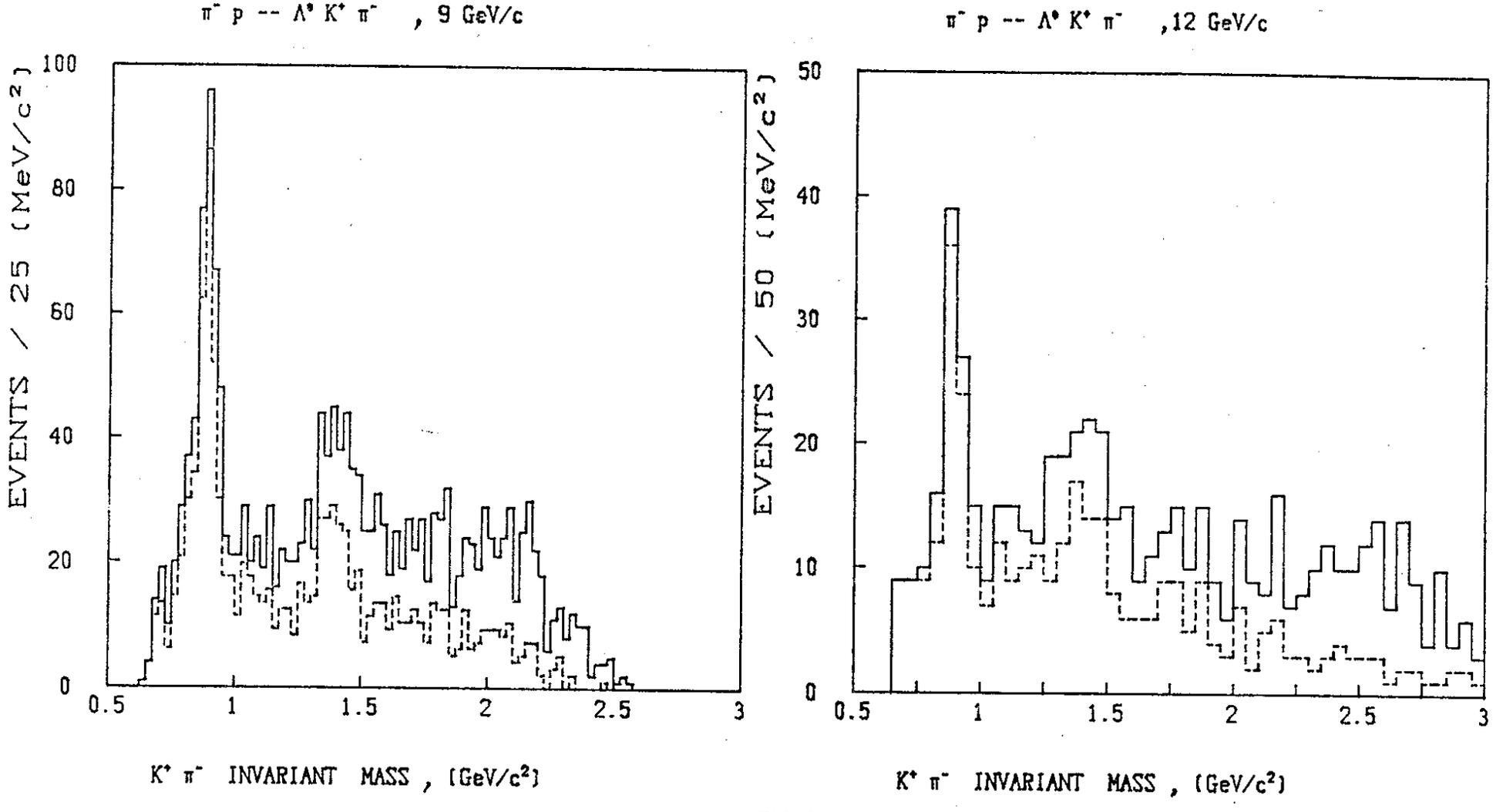
π⁻ p -- Λ° K⁺ π⁻ , 9 GeV/c
EVENTS / 25 (MeV/c²)
100
80
60
40
20
0
0.5
1
1.5
2
2.5
3
K⁺ π⁻ INVARIANT MASS , (GeV/c²)
π⁻ p -- Λ° K⁺ π⁻ ,12 GeV/c
EVENTS / 50 (MeV/c²)
50
40
30
20
10
0
0.5
1
1.5
2
2.5
3
K⁺ π⁻ INVARIANT MASS , (GeV/c²)

FIG. 4

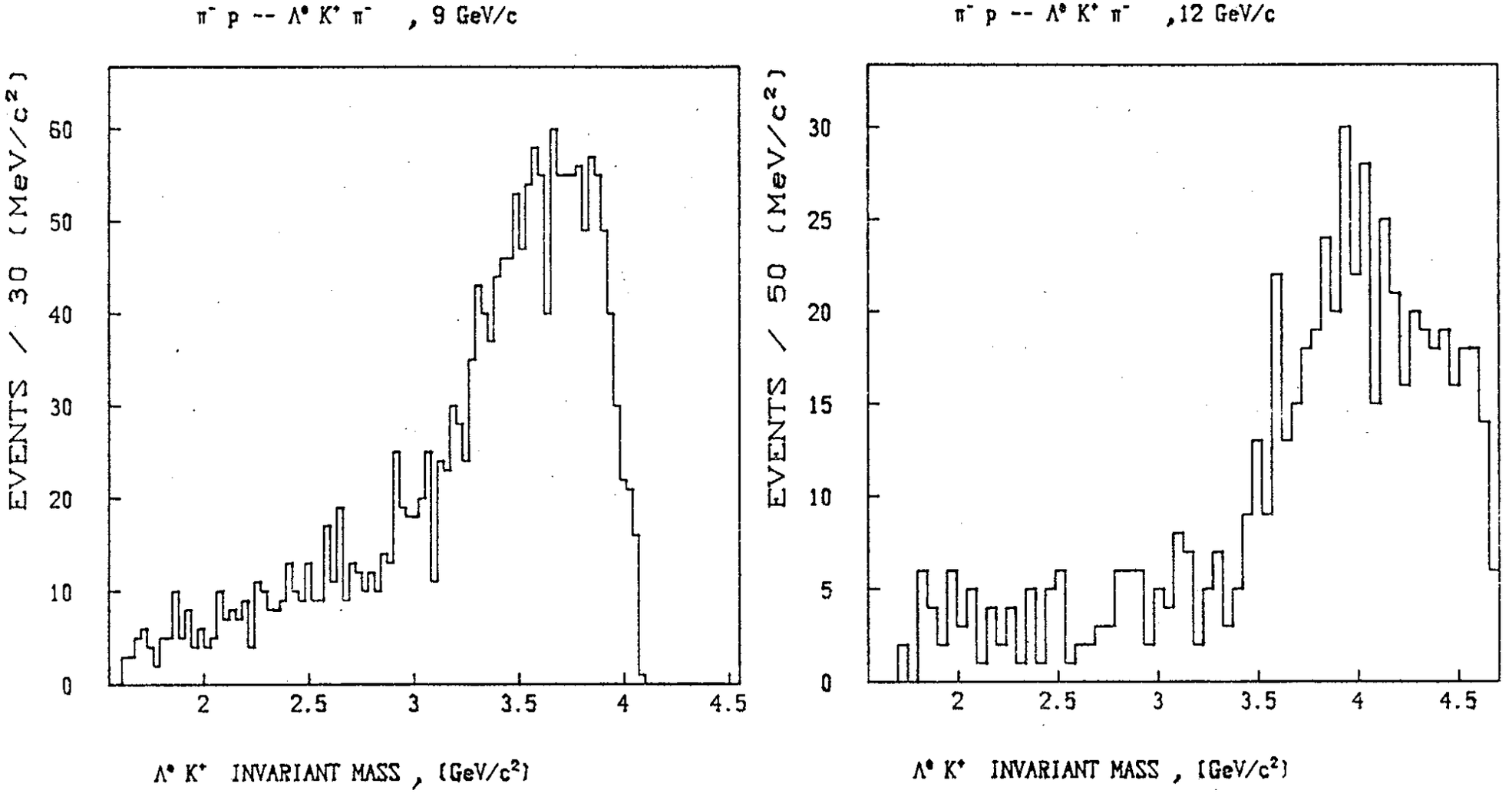
π⁻ p -- Λ° K⁺ π⁻ , 9 GeV/c
EVENTS / 30 (MeV/c²)
0
10
20
30
40
50
60
2
2.5
3
3.5
4
4.5
Λ° K⁺ INVARIANT MASS , (GeV/c²)
π⁻ p -- Λ° K⁺ π⁻ ,12 GeV/c
EVENTS / 50 (MeV/c²)
0
5
10
15
20
25
30
2
2.5
3
3.5
4
4.5
Λ° K⁺ INVARIANT MASS , (GeV/c²)

FIG.5

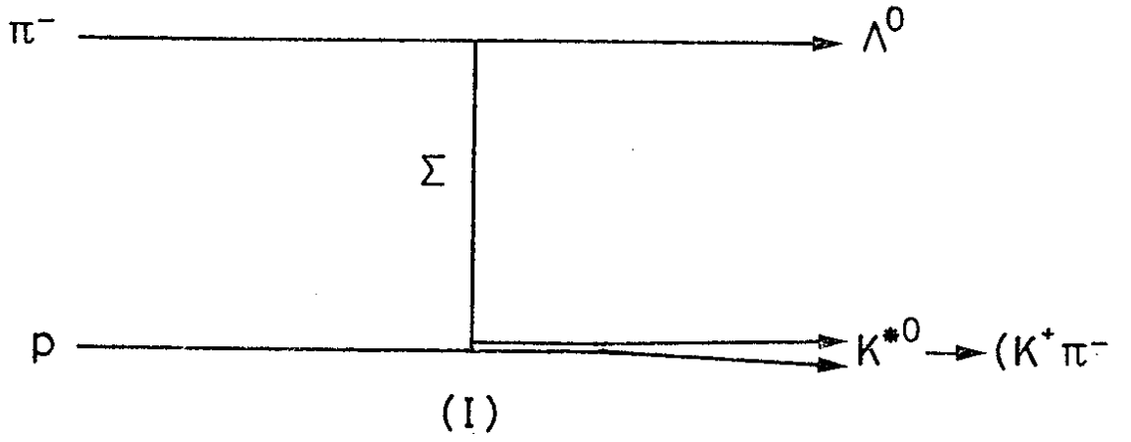

FIG. 6

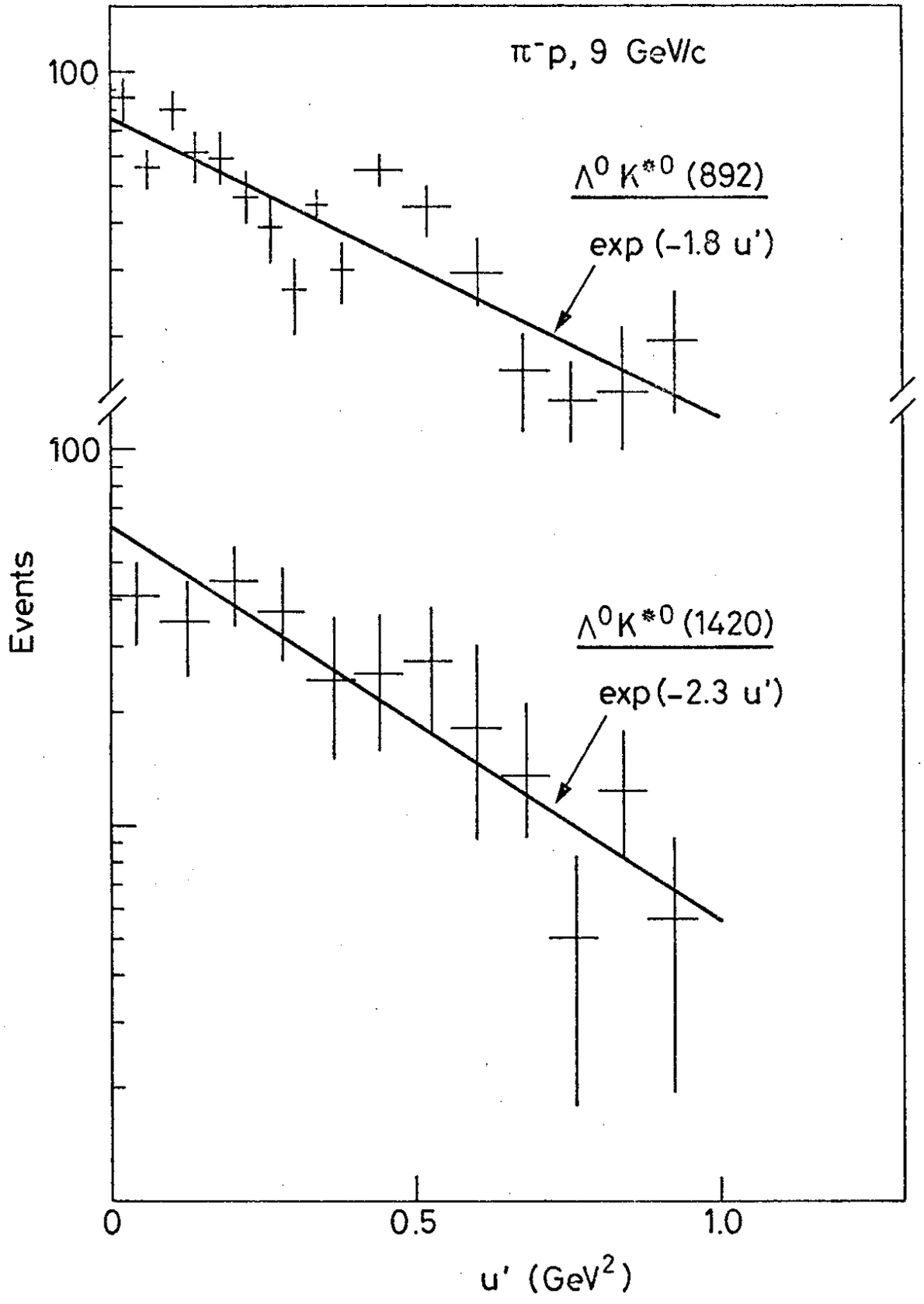
π⁻p, 9 GeV/c
100
Λ⁰ K*⁰ (892)
exp (−1.8 u')
100
Λ⁰K*⁰ (1420)
exp (−2.3 u')
Events
0
0.5
1.0
u' (GeV²)

FIG. 7

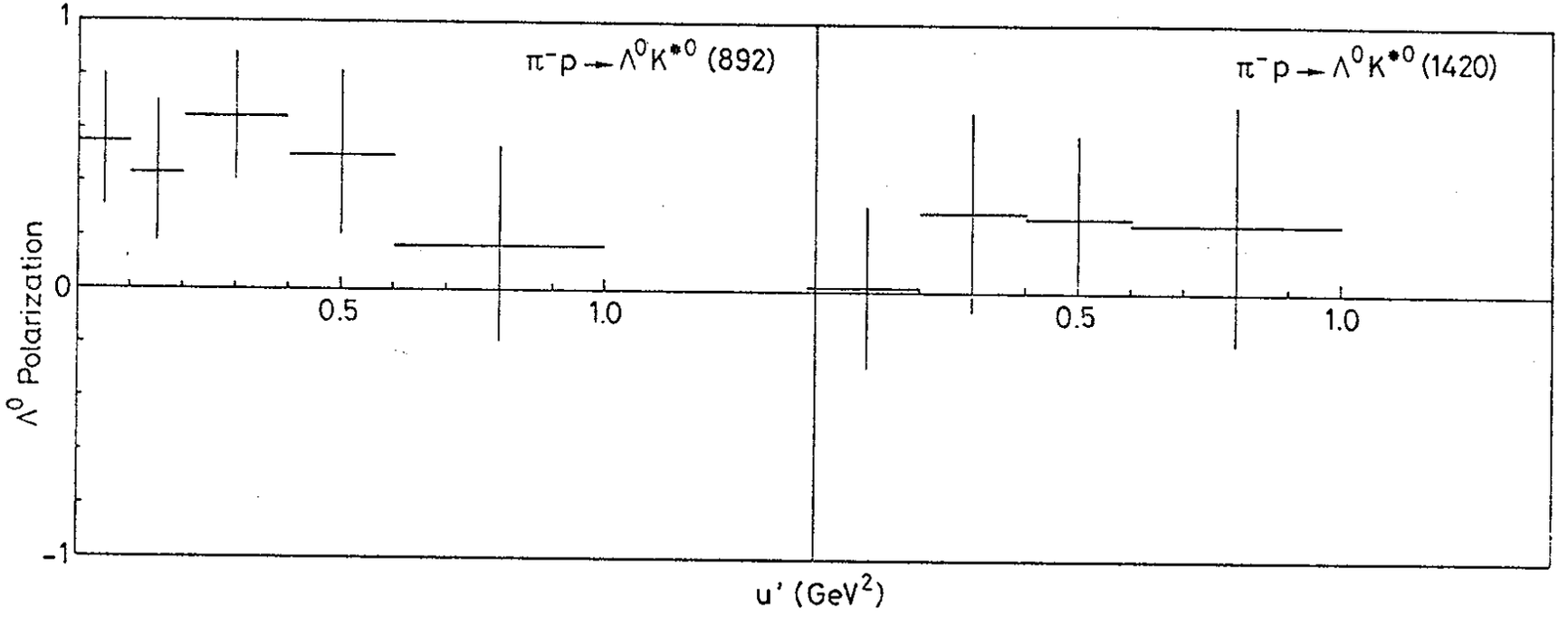
1
0
-1
Λ^0 Polarization
$\pi^- p \to \Lambda^0 K^{*0}$ (892)
$\pi^- p \to \Lambda^0 K^{*0}$ (1420)
0.5
1.0
0.5
1.0
u' (GeV^2)

FIG. 8

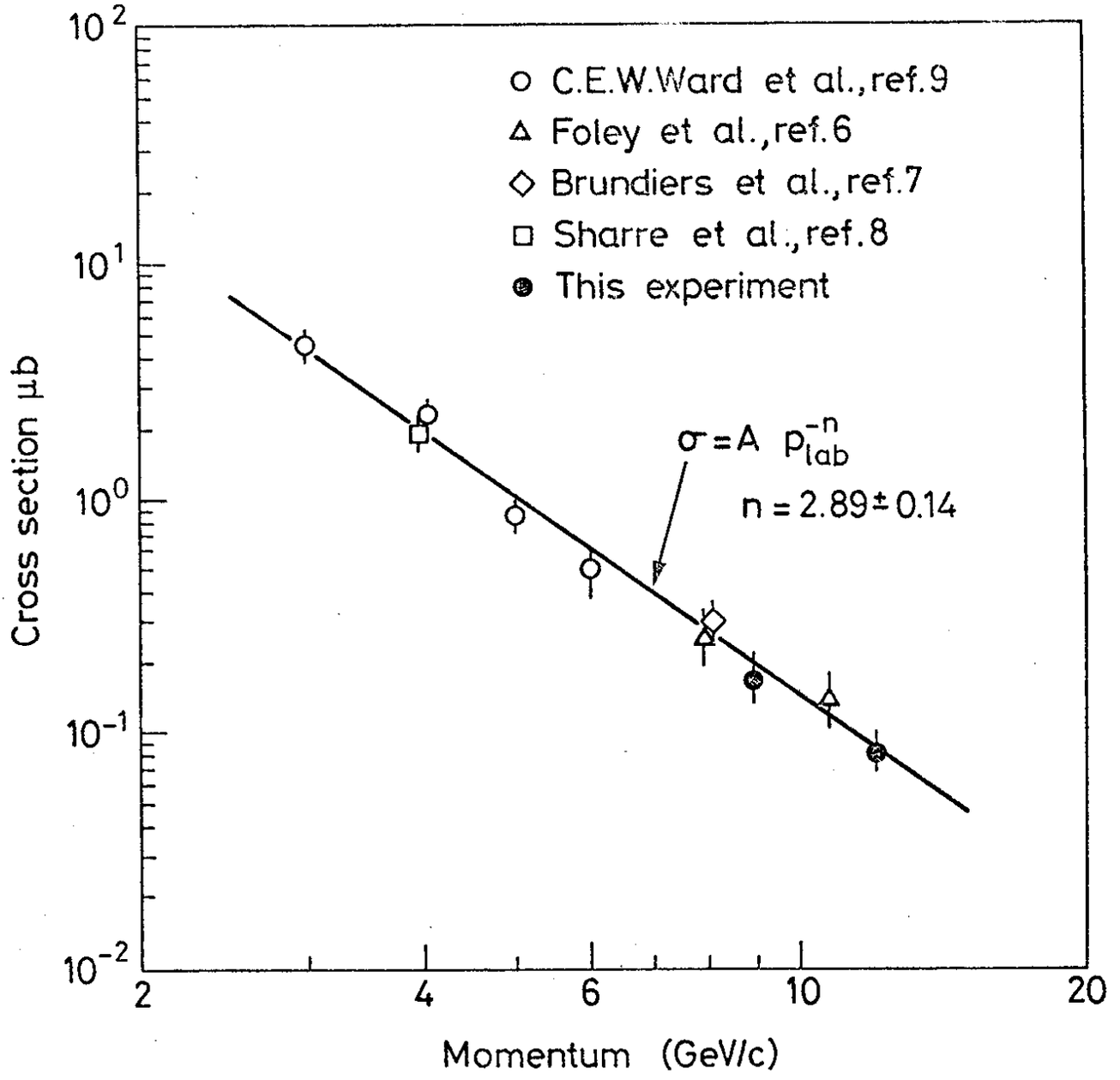
10 2
10 1
10 0
10 -1
10 -2
Cross section μb
2
4
6
10
20
Momentum (GeV/c)
○ C.E.W.Ward et al., ref.9
△ Foley et al., ref.6
◇ Brundiers et al., ref.7
□ Sharre et al., ref.8
● This experiment
σ = A p_lab^-n
n = 2.89 ± 0.14

FIG. 9

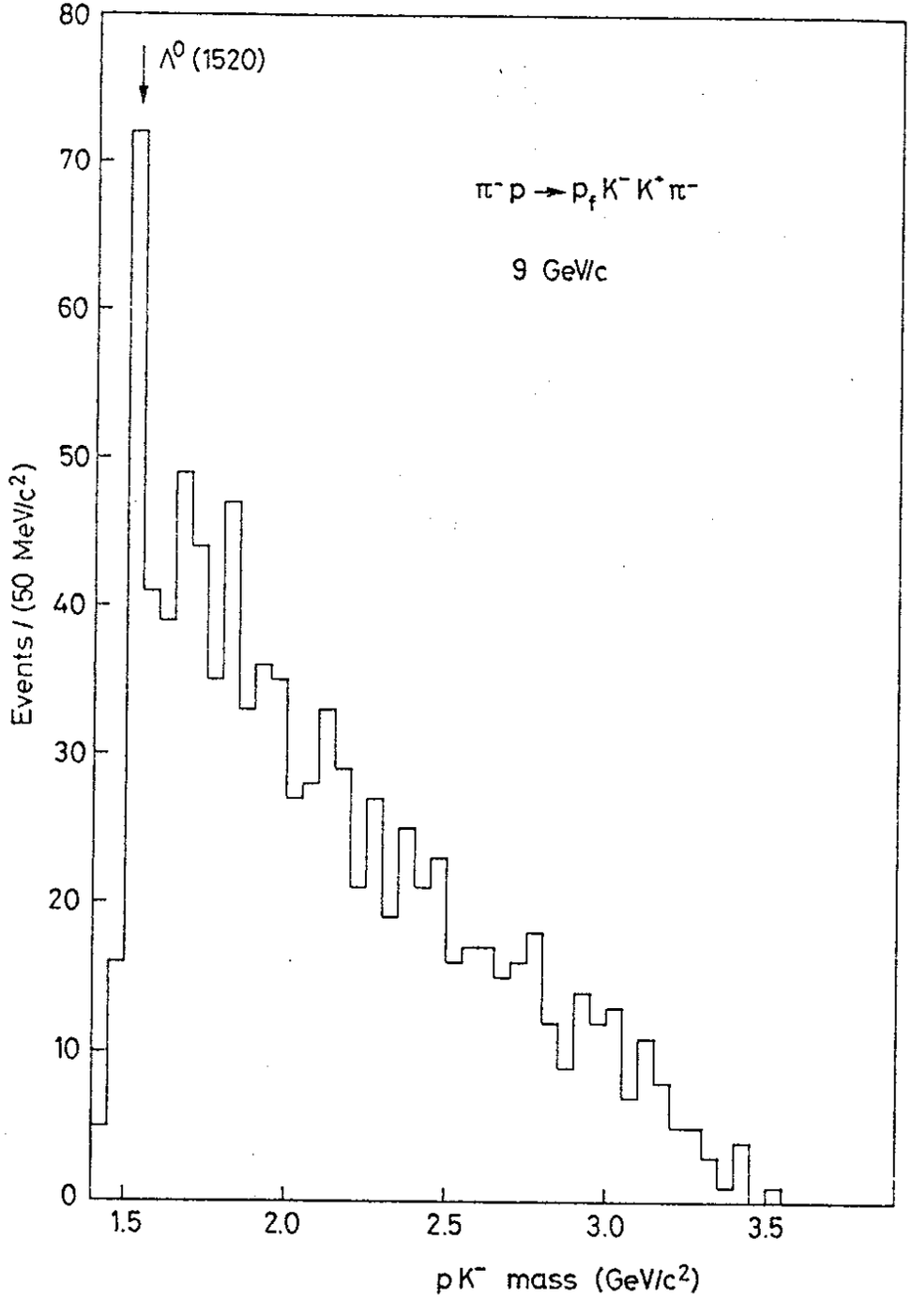
Λ⁰ (1520)
π⁻ p → p_f K⁻ K⁺ π⁻
9 GeV/c
Events / (50 MeV/c²)
p K⁻ mass (GeV/c²)

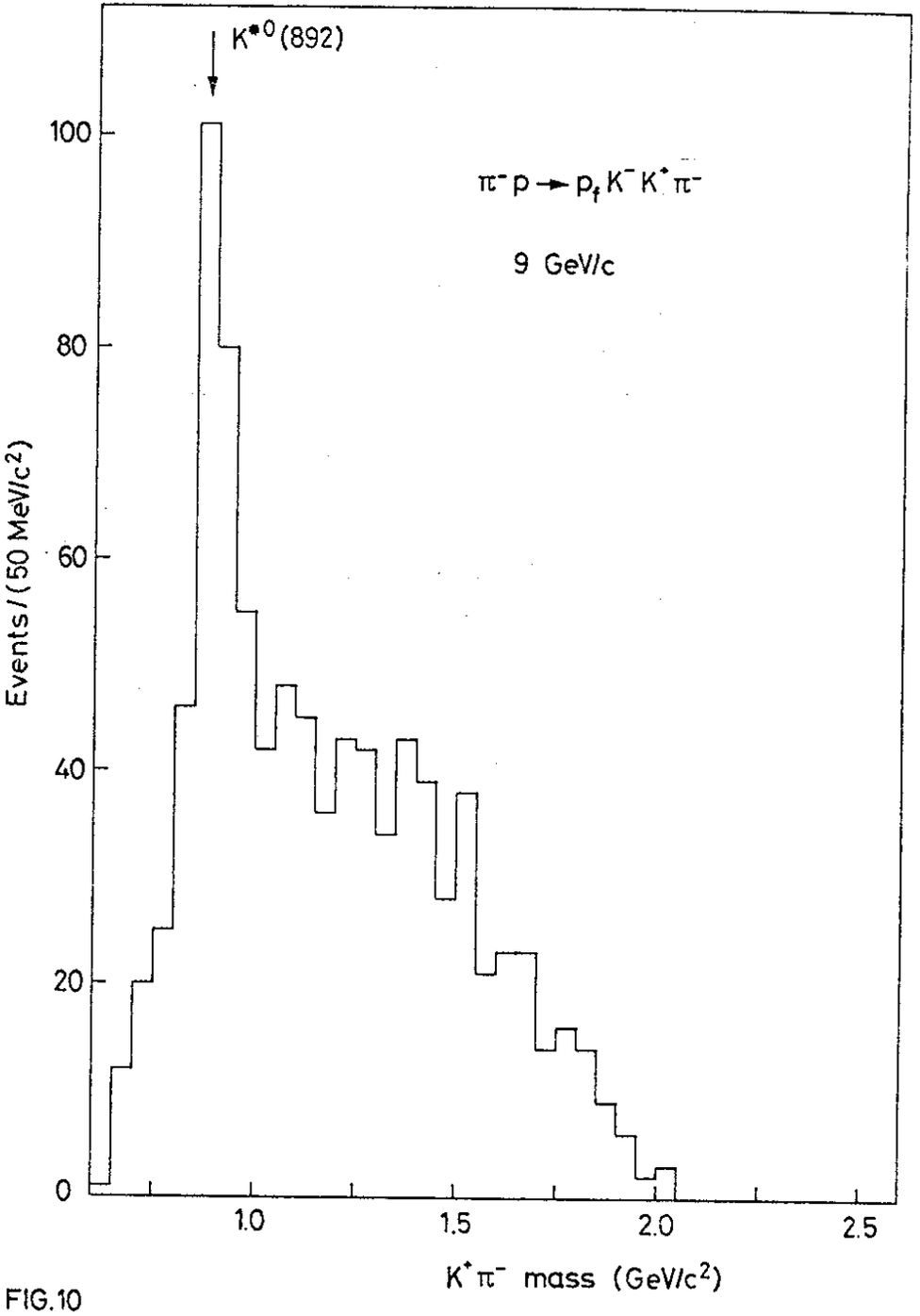
K*⁰(892)
π⁻ p → p_f K⁻ K⁺ π⁻
9 GeV/c
Events / (50 MeV/c²)
K⁺ π⁻ mass (GeV/c²)

FIG.10

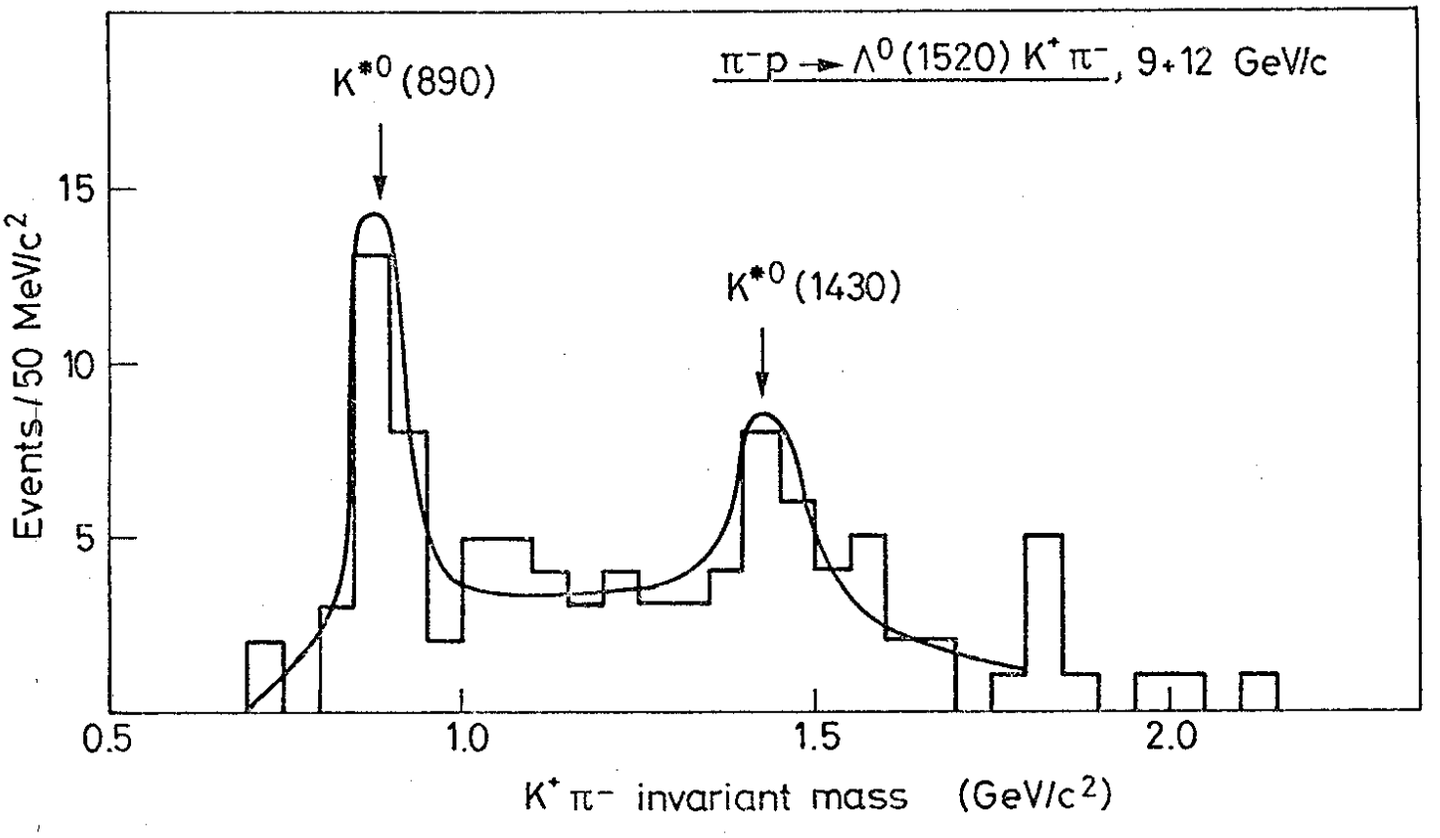
$\pi^- p \to \Lambda^0(1520)\, K^+\pi^-$, 9÷12 GeV/c
$K^{*0}(890)$
$K^{*0}(1430)$
Events/50 MeV/c^2
15
10
5
0.5
1.0
1.5
2.0
$K^+\pi^-$ invariant mass (GeV/c^2)

FIG. 11